

# A Simplified Analysis of the Tire-Tread Contact Problem using Displacement Potential Based Finite-Difference Technique

S Reaz Ahmed<sup>1</sup> and S K Deb Nath<sup>1</sup>

**Abstract:** The paper presents a simplified analysis of stresses and deformations at critical sections of a tire-tread. Displacement potential formulation is used in conjunction with the finite-difference method to model the present contact problem. The solution of the problem is obtained for two limiting cases of the contact boundary – one allows the lateral slippage and the other conforms to the no-slip condition along the lateral direction. The influential effects of tire material and tread aspect-ratio are discussed. The reliability and accuracy of the solution is also discussed in light of comparison made with the usual computational approach.

**Keywords:** Stress analysis, tire-tread contact problem, displacement potential function, finite-difference method

## 1 Introduction

Reliable and accurate analysis of stresses in tire-tread sections is an important practical issue. Based on the results of stress analysis of tire-tread sections in contact with the road, a number of practical issues associated with the serviceability of tires can be solved. For example, a fatigue test program can be conducted using results from the stress analysis as input to study the law of damage growth and thereby develop models for life prediction of tires. In addition, the stress analysis of tire-tread sections is a pre-requisite to the prediction of optimum shapes of tire-treads for avoiding the lateral slippage between the tire and roads. Therefore, since the service life a tire primarily depends on the life of treads, a careful analysis of stresses at the critical transition areas of tire-tread sections is of great practical importance for their improved design and thus improved life.

The elasticity problems are usually formulated using differential equations. Eventually, the solutions of the differential equations are required in order to obtain the

---

<sup>1</sup> Department of Mechanical Engineering, Bangladesh University of Engineering and Technology, Dhaka 1000, Bangladesh, E-mail: reaz207@yahoo.com

deformation and the state of stresses in the body. Analytical methods of solution are found to be inadequate for analyzing the practical problems of elasticity because of the complexity associated with the boundary conditions, materials and geometry. As a result, the numerical techniques are the most plausible approaches to deal with such problems, which generally include finite difference method (FDM), finite element method (FEM), etc. Besides the wide applications of FDM and FEM, recently the use of boundary element methods (BEM) is being investigated for the solution of isotropic, anisotropic as well as functionally graded materials, some of which are cited in the reference (see Aliabadi, 2002; Criado *et al.*, 2007; Tan *et al.*, 2009). On the other hand, a considerable research in computational mechanics has been devoted to the development of meshless methods (see Atluri and Shen, 2002). In an attempt to deal with contact problems, a frictionless contact algorithm for meshless methods was proposed by Vignjevic *et al.* (2006). One of the important paths in the evolution of meshless methods has been the development of the generalized (meshless) finite difference method (GFDM), which has also been applied to improve the approximated solutions of partial differential equations (Benito *et al.*, 2008). Instead of the differential formulation, an algebraic formulation of elastostatics, namely the Cell method has been reported (Tonti and Zarantonello, 2009), which avoids the discretization process of the differential equations. A stabilized radial basis functions collocation scheme has been proposed for boundary value problems subjected to mixed Neumann and Dirichlet boundary conditions (Libre *et al.*, 2008). A special set of mixed uniform boundary condition has however been proposed for evaluating the macroscopic elasticity tensor of human trabecular bone as well as for predicting the mechanical behavior of elastic and inelastic discontinuously reinforced composites (Pahr and Zysset, 2008; Pahr and Böhm, 2008).

Technical reporting on the analysis and design of rubber tires for various automotive vehicles is quite extensive in the literature. A number of authors have focused on the analysis of stresses and deformed shapes of reinforced tires by finite element method (Tabaddor and Stafford, 1985; Huh and Kwak, 1990; Wang *et al.*, 1996; Rothert and Gall, 1986). Some of the papers (Wang *et al.*, 1996; Rothert and Gall, 1986) considered the static tire contact problem for obtaining the deformation patterns and stress-state in the tire cross-section without paying attention to the bending effect of the reinforced cords. Taking the bending effect into consideration and laying emphasis on it during shear deformation of elements, Huh and Kwak (1990) developed the expressions of effective material properties of rubber composites, and applied to the inflation and contact problem of reinforced tire. Wang *et al.* (1996) reported an experimental stress-strain analysis by means of the Moire method in the area of the shoulder region of a retreaded tire section. They also presented a comparison of the experimental results with those obtained by FEM.

The specimen for the experiment was a cross-sectional slice of a retreaded truck tire. For the finite element comparison, a 2-D quarter tire model was created to best simulate the experimental condition. The tire section was modeled using three and four noded plane stress elements; rubber elements were modeled with isotropic, linear elastic and nearly incompressible properties. They reported that although the FEM results were in substantial agreement with the corresponding experimental results, the discrepancies were primarily because of the inability of satisfying the actual boundary conditions of experiment in the finite-element modeling of the problem. A number of computational algorithms have also been reported for solving contact problems involving sticking, frictional sliding, and separation between two bodies (Bathe and Chaudhary, 1984; Campos *et al.*, 1982; Oden *et al.*, 1984; Noor and Tanner, 1985; Oden and Pires, 1983). In most of these algorithms, the classical Coulomb's law of friction is used in the evaluation of tangential traction from the normal traction. A number of recent researchers are also found to show their interest in the stress analysis of multi-layered and multi-laminated system of truck/tractor tires using non-linear finite-element analysis, some of which are cited in the reference (see Zhang *et al.*, 2002; Mohenimanesh *et al.*, 2009).

In the present paper, an ideal mathematical model for the boundary-value stress problems, namely, the displacement potential formulation (Ahmed *et al.*, 1996; Ahmed *et al.*, 1998) has been used in conjunction with finite-difference method to analyze the deformed shape as well as stresses in the tire-tread sections. This boundary modeling approach has generated much renewed interest in the field of numerical and analytical solutions of mixed-boundary-value problems in solid mechanics (Akanda *et al.*, 2002; Ahmed *et al.*, 2005a; Nath and Ahmed, 2009). It is important to note that the present mathematical model permits reduction of parameters to be evaluated at each nodal point to one, whereas the standard methods of solution need at least two unknowns to be evaluated at each nodal point for the solution of a two-dimensional problem. As a result, the total number of equations to be solved is much less in the present approach, which, in turn, leads to the reduction of computational effort as well as improves the quality of solution (Ahmed *et al.*, 2005a). Moreover, the use of finite-difference technique is considered to be especially suitable for the present case, as the investigation concentrates primarily on the prediction of stresses at the surfaces of tire-treads. In this context, it can be mentioned that the superiority of finite-difference method of solution in predicting the surface stresses has been verified in our earlier researches and also by the investigation of Dow *et al.* (1990). Recently, a new numerical method of analysis has been proposed to determine the optimum shapes of tire treads for avoiding lateral slippage between tires and roads (Ahmed *et al.*, 2005b).

Considering the tire-tread problem as a mixed-boundary-value plane problem of

linear elasticity, the numerical solutions are obtained for the deformation and stresses at different sections of the treads, specifically at the contact surface and the intersecting section of tire and treads (shoulder). Solutions are obtained for the two limiting cases of the contact surface – one allows free lateral slippage and the other conforms to the no-slip condition of the boundary. In the first case, the contact surface is assumed to be free from any frictional resistance from the road, which allows free slippage of the surface on the road in the direction perpendicular to the direction of vehicular motion (lateral direction), under the influence of a uniform contact pressure (see Fig. 1). On the other hand, the no-slip condition of the tread conforms to the situation where the frictional resistance from the road is sufficiently high to prevent the lateral slippage of the contact surface. It is noted here that the friction in the direction of vehicular motion can hardly contribute to the abrasion loss of treads as far as the rotary motion of the tire is concerned. The lateral slippage on the road surface has however been identified to be one of the major reasons for shortening the life of tires as far as abrasion loss is concerned (Ahmed *et al.*, 2005b). In an attempt to make the results useful for practical applications, for both the cases of contact surface, solutions are obtained for actual truck tire rubber as well as commercially available natural rubber. The no-slip shearing stress at the contact boundary is also analyzed in an attempt to predict the frictional resistance required to keep the contact boundary free from the lateral slippage on the road. Finally, the reliability and accuracy of the present displacement potential solution is discussed in light of comparison made with that of the usual computational method.

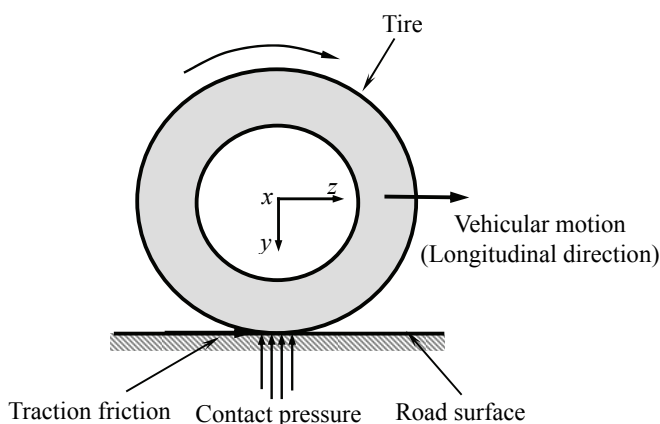


Figure 1: Direction of motion of tire with traction friction on tire treads

## 2 Displacement Potential Formulation

With reference to a rectangular coordinate system, in absence of body forces, the governing equations of equilibrium for the plane problems of isotropic, elastic bodies of Hookean materials, in terms of displacement components, are as follows (Ahmed *et al.*, 1998; Timoshenko, 1979)

$$\frac{\partial^2 u_x}{\partial x^2} + \frac{1+\mu}{2} \frac{\partial^2 u_y}{\partial x \partial y} + \frac{1-\mu}{2} \frac{\partial^2 u_x}{\partial y^2} = 0 \quad (1)$$

$$\frac{\partial^2 u_y}{\partial y^2} + \frac{1+\mu}{2} \frac{\partial^2 u_x}{\partial x \partial y} + \frac{1-\mu}{2} \frac{\partial^2 u_y}{\partial x^2} = 0 \quad (2)$$

where,  $\mu$  is the Poisson's ratio of the material. The stress components are calculated from the following stress-displacement relations (Timoshenko, 1979):

$$\sigma_{xx} = \frac{E}{1-\mu^2} \left[ \frac{\partial u_x}{\partial x} + \mu \frac{\partial u_y}{\partial y} \right] \quad (3)$$

$$\sigma_{yy} = \frac{E}{1-\mu^2} \left[ \frac{\partial u_y}{\partial y} + \mu \frac{\partial u_x}{\partial x} \right] \quad (4)$$

$$\sigma_{xy} = \frac{E}{2(1+\mu)} \left[ \frac{\partial u_x}{\partial y} + \frac{\partial u_y}{\partial x} \right] \quad (5)$$

In the displacement potential formulation, the displacement components are expressed in terms of a potential function  $\psi$  of space variables as follows (Ahmed *et al.*, 2005a):

$$u_x = \alpha_1 \frac{\partial^2 \psi}{\partial x^2} + \alpha_2 \frac{\partial^2 \psi}{\partial x \partial y} + \alpha_3 \frac{\partial^2 \psi}{\partial y^2} \quad (6)$$

$$u_y = \alpha_4 \frac{\partial^2 \psi}{\partial x^2} + \alpha_5 \frac{\partial^2 \psi}{\partial x \partial y} + \alpha_6 \frac{\partial^2 \psi}{\partial y^2} \quad (7)$$

Here,  $\alpha_i$  are material constants.

Combining the equations (1), (2), (6) and (7), we obtain the equilibrium equations in terms of the function  $\psi(x, y)$ , which are

$$\begin{aligned} & \alpha_1 \frac{\partial^4 \psi}{\partial x^4} \\ & + \left\{ \alpha_2 + \alpha_4 \left( \frac{1+\mu}{2} \right) \right\} \frac{\partial^4 \psi}{\partial x^3 \partial y} + \left\{ \alpha_3 + \alpha_1 \left( \frac{1-\mu}{2} \right) + \alpha_5 \left( \frac{1+\mu}{2} \right) \right\} \frac{\partial^4 \psi}{\partial x^2 \partial y^2} \\ & + \left\{ \alpha_2 \left( \frac{1-\mu}{2} \right) + \alpha_6 \left( \frac{1+\mu}{2} \right) \right\} \frac{\partial^4 \psi}{\partial x \partial y^3} + \alpha_3 \left( \frac{1-\mu}{2} \right) \frac{\partial^4 \psi}{\partial y^4} = 0 \quad (8) \end{aligned}$$

$$\begin{aligned} & \alpha_4 \left( \frac{1-\mu}{2} \right) \frac{\partial^4 \psi}{\partial x^4} + \left\{ \alpha_1 \left( \frac{1+\mu}{2} \right) + \alpha_5 \left( \frac{1-\mu}{2} \right) \right\} \frac{\partial^4 \psi}{\partial x^3 \partial y} \\ & + \left\{ \alpha_3 \left( \frac{1+\mu}{2} \right) + \alpha_5 \right\} \frac{\partial^4 \psi}{\partial x \partial y^3} + \left\{ \alpha_2 \left( \frac{1+\mu}{2} \right) + \alpha_4 + \alpha_6 \left( \frac{1-\mu}{2} \right) \right\} \frac{\partial^4 \psi}{\partial x^2 \partial y^2} \\ & + \alpha_6 \frac{\partial^4 \psi}{\partial y^4} = 0 \quad (9) \end{aligned}$$

The constants,  $\alpha$ 's are chosen here in such a way that Eq. (8) is automatically satisfied under all circumstances. This will happen when coefficients of all the derivatives present in Eq. (8) are individually zero.

Thus, for  $\psi$  to be a solution of the stress problem, it has to satisfy Eq. (9) only. However, the values of  $\alpha$ 's must be known in advance. It has been shown that, for isotropic solids the values of the material constants,  $\alpha$ 's are given by the following expressions (Ahmed *et al.*, 2005a):

$$\alpha_1 = \alpha_3 = \alpha_5 = 0$$

$$\alpha_2 = 1$$

$$\alpha_4 = -\frac{2}{1+\mu} \quad (10)$$

$$\alpha_6 = -\frac{1-\mu}{1+\mu}$$

When the above values of  $\alpha$ 's are substituted in Eq. (8), it is automatically satisfied, and thus the governing difference equation (Eq. 9) for the solution of two-dimensional problem becomes

$$\frac{\partial^4 \psi}{\partial x^4} + 2 \frac{\partial^4 \psi}{\partial x^2 \partial y^2} + \frac{\partial^4 \psi}{\partial y^4} = 0 \quad (11)$$

The problem is thus reduced to the evaluation of a single function  $\psi(x, y)$  from the single governing equation of equilibrium (Eq. 11), along with the specified boundary conditions. Thus, the computational work in solving any problem remains the same in the present case as it was in the case of stress function formulation (Timoshenko, 1979), since both of them have to satisfy the same bi-harmonic partial differential equation. But the  $\psi$ -formulation is free from the inability of the stress function formulation in handling the mixed boundary conditions.

### 2.1 Expressions of boundary conditions in terms of the function, $\psi$

Combining Eqs. (3) to (7) and (10), the expressions for the body parameters in terms of the function  $\psi(x, y)$  can be obtained as follows (Ahmed *et al.*, 1998):

$$u_x(x, y) = \frac{\partial^2 \psi}{\partial x \partial y} \quad (12)$$

$$u_y(x, y) = -\frac{1}{1+\mu} \left[ 2 \frac{\partial^2 \psi}{\partial x^2} + (1-\mu) \frac{\partial^2 \psi}{\partial y^2} \right] \quad (13)$$

$$\sigma_{xx}(x, y) = \frac{E}{(1+\mu)^2} \left[ \frac{\partial^3 \psi}{\partial x^2 \partial y} - \mu \frac{\partial^3 \psi}{\partial y^3} \right] \quad (14)$$

$$\sigma_{yy}(x, y) = -\frac{E}{(1+\mu)^2} \left[ (2+\mu) \frac{\partial^3 \psi}{\partial x^2 \partial y} + \frac{\partial^3 \psi}{\partial y^3} \right] \quad (15)$$

$$\sigma_{xy}(x, y) = -\frac{E}{(1+\mu)^2} \left[ \frac{\partial^3 \psi}{\partial x^3} - \mu \frac{\partial^3 \psi}{\partial x \partial y^2} \right] \quad (16)$$

The boundary conditions at any point on the boundary are known in terms of normal and tangential components of displacement and stress. The expressions for the normal and tangential components of displacement, in terms of the function, are (Akanda *et al.*, 2002)

$$u_n(x, y) = -\frac{2}{1+\mu} m \frac{\partial^2 \psi}{\partial x^2} + l \frac{\partial^2 \psi}{\partial x \partial y} - \frac{1-\mu}{1+\mu} m \frac{\partial^2 \psi}{\partial y^2} \quad (17)$$

$$u_t(x, y) = \frac{2}{1+\mu} l \frac{\partial^2 \psi}{\partial x^2} + m \frac{\partial^2 \psi}{\partial x \partial y} + \frac{1-\mu}{1+\mu} l \frac{\partial^2 \psi}{\partial y^2} \quad (18)$$

where,  $l$  and  $m$  are the direction cosines of a point on the boundary. Similarly, the corresponding expressions for the normal and tangential components of stress for points on the boundary are (Akanda *et al.*, 2002),

$$\begin{aligned} \sigma_n(x, y) = \frac{E}{(1+\mu)^2} \left[ -2lm \frac{\partial^3 \psi}{\partial x^3} + (l^2 - 2m^2 + \mu m^2) \frac{\partial^3 \psi}{\partial x^2 \partial y} \right. \\ \left. + 2lm \frac{\partial^3 \psi}{\partial x \partial y^2} - (\mu l^2 + m^2) \frac{\partial^3 \psi}{\partial y^3} \right] \quad (19) \end{aligned}$$

$$\begin{aligned} \sigma_t(x, y) = \frac{E}{(1+\mu)^2} \left[ (l^2 - m^2) \frac{\partial^3 \psi}{\partial x^3} + lm(3+\mu) \frac{\partial^3 \psi}{\partial x^2 \partial y} - \mu(l^2 - m^2) \frac{\partial^3 \psi}{\partial x \partial y^2} \right. \\ \left. + lm(1-\mu) \frac{\partial^3 \psi}{\partial y^3} \right] \quad (20) \end{aligned}$$

As appears from the above expressions, all the boundary conditions of interest can readily be discretized in terms of the function  $\psi$  by the method of finite-difference. The distinguishing feature of the present formulation is that, a single function has to be evaluated at each mesh point instead of solving for at least two variables simultaneously as in the case of standard method of solution. Moreover, all modes of boundary conditions can be satisfied appropriately, whether they are specified in terms of loading or physical restraints or any combination thereof. It is noted that the reliability as well as superiority of the  $\psi$ -formulation has been verified repeatedly through the analytical and numerical solutions of a number of mixed-boundary-value stress problems of solid mechanics (Ahmed *et al.*, 1996; Ahmed *et al.*, 1998; Akanda *et al.*, 2002; Ahmed *et al.*, 2005a; Nath and Ahmed, 2009).

### 3 Numerical Modeling of the Problem

#### 3.1 Method of solution

The limitation and complexity associated with the analytical method of solution ultimately leads to the conclusion that a numerical modeling for the present problem is the only plausible approach. Finite-difference technique is used to discretize the governing differential equation (11) and also the differential equations associated with the boundary conditions (Eq. (17)-(20)). The discrete values of the displacement potential function  $\psi(x,y)$ , at the mesh points of the domain concerned, is solved from the system of linear algebraic equations resulting from the discretization of the governing equation of equilibrium and the associated boundary conditions.

#### 3.2 Discretization of the computational field

According to the usual practice, the region in which a dependent function is to be evaluated is divided into a desirable number of mesh points and the values of the function are sought only at these mesh points. The present program is to solve a function within a stepped rectangular region, as shown in Fig. 2, which is divided into meshes with lines parallel to rectangular coordinate axes. Considering the rectangular shape of the boundary and also the nature of the differential equations involved, a uniform rectangular mesh-network is thus used to model the present tire-tread problem. The present domain of the tread is discretized with a minimum of  $(28 \times 18)$  nodal points, and the corresponding stability as well as accuracy of the present finite-difference solution is checked by varying the mesh density. The discretization scheme of the tread section is schematically illustrated in Figure 3.

The governing differential equation, which is used to evaluate the function  $\psi$  only at the internal mesh points, is expressed in its corresponding difference form using

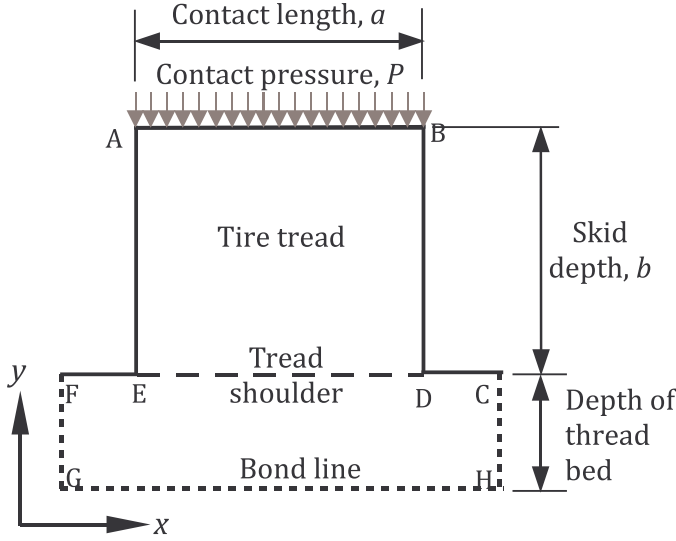


Figure 2: Loading and geometry of a typical tire-tread section

central difference operators. When all the derivatives present in the bi-harmonic equation (11) are replaced by their respective central difference formulae, the complete finite-difference expression for the governing equation of equilibrium becomes

$$R^4 \{ \psi(i-2, j) + \psi(i+2, j) \} - 4R^2(1 + R^2) \{ \psi(i-1, j) + \psi(i+1, j) \} - 4(1 + R^2) \{ \psi(i, j+1) + \psi(i, j-1) \} + (6R^4 + 8R^2 + 6) \psi(i, j) + 2R^2 \{ \psi(i-1, j-1) + \psi(i-1, j+1) + \psi(i+1, j-1) + \psi(i+1, j+1) \} + \psi(i, j-2) + \psi(i, j+2) = 0 \quad (21)$$

where,  $R = k/h$ .

The corresponding grid structure of the difference equation (21) for any internal mesh point  $(i, j)$  is shown in Fig. 3. The pivotal point  $(i, j)$  in the grid structure is the point of application of the governing equation. For the case of any interior mesh point, the finite-difference equation (21) contains the discretized variable of the thirteen neighboring mesh points, and when the point of application  $(i, j)$  becomes an immediate neighbor of the physical boundary, the equation will involve mesh points both interior and exterior to the physical boundary as shown in Fig. 3. Thus, an imaginary boundary, exterior to the physical boundary of the tread domain, as shown in Fig. 3, is introduced so that the application of the central-difference stencil of the governing equation, especially to the points in the immediate neighbor of the

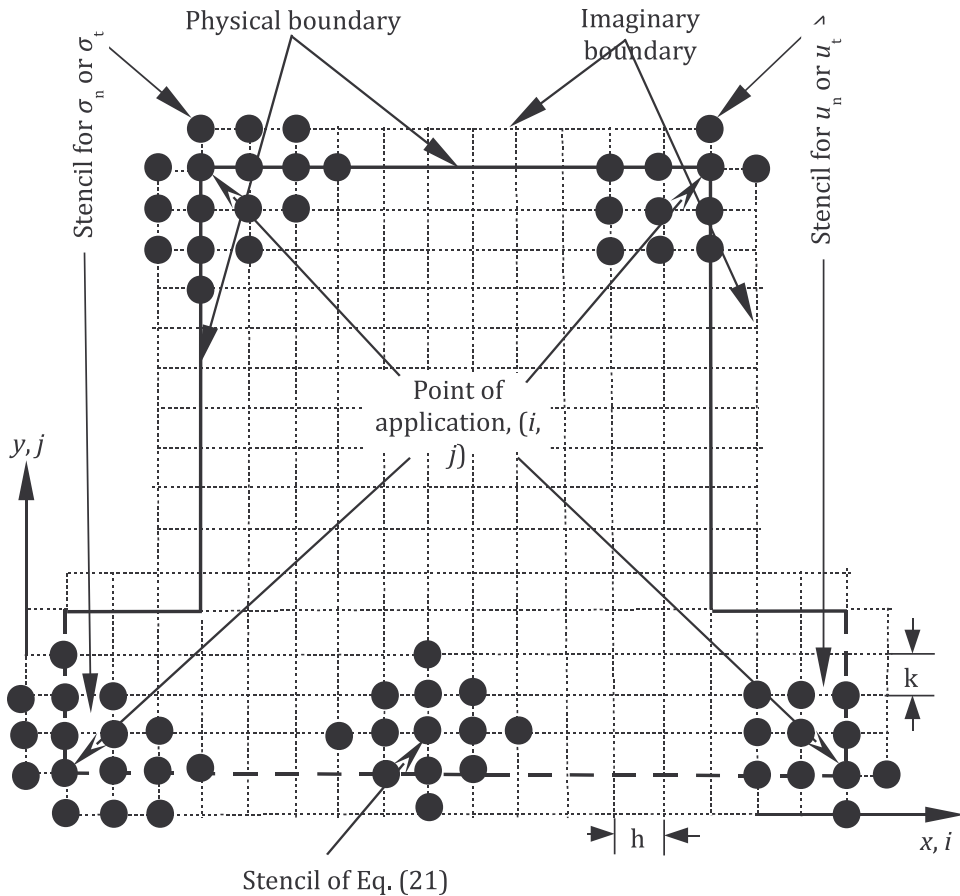


Figure 3: Application of the stencils of different boundary conditions and governing equation at different points of the tread section

physical boundary, causes no difficulties.

### 3.3 Management of boundary conditions

As the differential equations associated with the boundary conditions contain second and third order derivatives of the function  $\psi$ , the use of central-difference expressions is not practical as, most of the time, it leads to the inclusion of points exterior to the imaginary boundary. The derivatives of the boundary expressions are thus replaced by their corresponding backward or forward difference formulae, keeping the order of the local truncation error the same ( $O(h^2)$ ). Further, the same forward or backward difference formula cannot be used for different segments of

the boundary, as it includes points exterior to the imaginary boundary. In order to meet the requirement, four different sets of finite-difference expressions for each of the boundary conditions are used for the points at different regions on the boundary. These four sets of algebraic equations are derived by adopting the  $i$ -forward &  $j$ -forward,  $i$ -forward &  $j$ -backward,  $i$ -backward &  $j$ -forward, and  $i$ -backward &  $j$ -backward finite-difference schemes. The choice of the appropriate set of expressions for a point on the boundary is determined by its position on the boundary, which will avoid the occurrence of additional mesh points external to the imaginary boundary. For example, the finite-difference expressions of the boundary conditions for the bottom-left segment of the boundary are obtained by using the  $i$ -forward and  $j$ -forward difference formulae for the derivatives (see Fig. 3). For points on the bottom-left segment of the boundary, the finite-difference expressions of the normal components of displacement and stress are expressed as

$$\begin{aligned} u_n(i, j) = & Y_1 \psi(i, j) + Y_2 \psi(i-1, j) + Y_3 \psi(i, j-1) + Y_4 \psi(i, j+1) + Y_5 \psi(i+1, j+2) \\ & + Y_6 \psi(i+1, j+1) + Y_7 \psi(i+1, j) + Y_8 \psi(i, j+2) + Y_9 \psi(i+2, j) \\ & + Y_{10} \psi(i+2, j+1) + Y_{11} \psi(i+2, j+2) \quad (22) \end{aligned}$$

$$\begin{aligned} \sigma_n(i, j) = & Z_1 \psi(i, j) + Z_2 \psi(i-1, j) + Z_3 \psi(i-1, j+1) + Z_4 \psi(i-1, j+2) \\ & + Z_5 \psi(i, j-1) + Z_6 \psi(i, j+1) + Z_7 \psi(i, j+2) + Z_8 \psi(i, j+3) + Z_9 \psi(i+1, j-1) \\ & + Z_{10} \psi(i+1, j) + Z_{11} \psi(i+1, j+1) + Z_{12} \psi(i+1, j+2) + Z_{13} \psi(i+2, j-1) \\ & + Z_{14} \psi(i+2, j) + Z_{15} \psi(i+2, j+1) + Z_{16} \psi(i+3, j) \quad (23) \end{aligned}$$

Similarly, the corresponding finite-difference equations for points on the top-right segment of the boundary, obtained by using the  $i$ -backward and  $j$ -backward difference formulae for the derivatives, are as follows:

$$\begin{aligned} u_n(i, j) = & Y_{12} \psi(i, j) + Y_{13} \psi(i+1, j) + Y_{14} \psi(i, j+1) + Y_{15} \psi(i, j-1) + Y_{16} \psi(i, j-2) \\ & + Y_{17} \psi(i-1, j-1) + Y_{18} \psi(i-1, j) + Y_{19} \psi(i-1, j-2) + Y_{20} \psi(i-2, j) \\ & + Y_{21} \psi(i-2, j-1) + Y_{22} \psi(i-2, j-2) \quad (24) \end{aligned}$$

$$\begin{aligned} \sigma_n(i, j) = & Z_{17} \psi(i, j) + Z_{18} \psi(i-1, j) + Z_{19} \psi(i-1, j+1) + Z_{20} \psi(i-1, j-1) \\ & + Z_{21} \psi(i-1, j-2) + Z_{22} \psi(i-2, j) + Z_{23} \psi(i-2, j+1) + Z_{24} \psi(i-2, j-1) \\ & + Z_{25} \psi(i-3, j) + Z_{26} \psi(i, j+1) + Z_{27} \psi(i, j-1) + Z_{28} \psi(i, j-2) \\ & + Z_{29} \psi(i, j-3) + Z_{30} \psi(i+1, j) + Z_{31} \psi(i+1, j-1) + Z_{32} \psi(i+1, j-2) \quad (25) \end{aligned}$$

where, the coefficients  $Y_i$  and  $Z_i$  are the functions of elastic constants ( $E$  and  $\mu$ ), mesh lengths ( $h$  and  $k$ ), and direction cosines of the boundary point ( $l$  and  $m$ ).

The discretization scheme using the neighboring field grid points as required for expressing the displacement and stress boundary conditions for different boundary segments are illustrated in Fig. 3.

### ***3.4 Placement of boundary conditions and evaluation of parameters of interest***

Since there are two conditions to be satisfied at a point on the physical boundary of the tread section, two difference equations corresponding to the respective boundary conditions are applied to the same point on the boundary. Out of these two equations, one is used to evaluate the function  $\psi$  at the physical boundary point and the remaining one for the corresponding point on the imaginary boundary. Therefore, the application of the governing equation as well as the necessary boundary conditions ensures that every mesh point of the computational domain will have a single algebraic equation for its evaluation.

Special treatments are adopted for the corner mesh points, which are generally the points of ‘transition’ in the boundary conditions. The geometry of the present tire tread section contains a total of eight corner points – six external and two internal corner points (for example, referring to the Fig. 2, A, B, C, D, G, H are external, and E, F are internal corner points). For the case of corner points, the available boundary conditions are usually more than that available for the remaining boundary points. In an attempt to deal with these singularities in a reasonable manner, a total of three out of the four conditions have been satisfied for all the external corner points and the remaining one is treated as redundant, which is in contrast with the usual computational approaches. For example, in the case of usual finite-element method of simulation, the corner points are not treated taking into account the effect of singularity, rather only two of the available four conditions are satisfied in obtaining the solutions. The two internal corner points, on the other hand, have basically two conditions, one of which has been used and the other is dropped for the sake of the present finite-difference management of the boundary conditions.

The discrete values of the potential function,  $\psi(x, y)$ , at every mesh point are solved from the system of linear algebraic equations resulting from the discretization of the governing equation and the associated boundary conditions, by using direct method of solution. To solve the system of equations, the authors used the triangular decomposition method for better reliability of solutions in a shorter period of time. Finally, in order to evaluate the parameters of interest in the solution of tire-tread problem, namely, the components of stress and displacement, four sets of finite-difference expressions for each of the equations (12)–(16) are developed in a fashion similar to that adopted in the case of boundary conditions. Since all the components of stress and displacement are expressed in terms of derivatives of the function  $\psi$ , the parameters of interest are readily calculated from the  $\psi$  values

obtained at the mesh points of the domain.

#### **4 Mechanical Properties of Tire Rubber**

In the present analysis, instead of using the available material properties of natural rubber, attempt has been made to determine the necessary material properties, namely the Poisson's ratio and the compression modulus of actual tire rubber, in our laboratory by simple experiments (Ahmed *et al.*, 2005b). Specimens were prepared from an original sample of brand new truck tire (Dunlop R.T.M. Supreme Tire, made in India). Test specimens were prepared from the tread region of the tire. The Poisson's ratio was calculated from the measured values of tension modulus and shear modulus of tire rubber. Typical dumbbell-shaped tension specimens were used to determine the tension modulus, whereas the compression modulus was obtained from the compression test of tread blocks. The shear modulus of tire rubber was determined from the tread blocks following the standard procedure mentioned in ASTM Standard D4014–89. All the experiments were repeated four times and the results were averaged. In an attempt to compare the obtained properties of truck tire rubber, the commercially available natural rubber was also investigated for the above mentioned properties.

The Poisson's ratio of tire rubber was obtained as 0.43, while that of natural rubber was found to take a value very close to its standard value, that is, 0.5. It should be mentioned here that the value of Poisson's ratio of tire rubber as used in their analysis of Tabaddor and Stafford (1985) and Huh and Kwak (1990) was 0.45 and 0.49, respectively. The tension and compression moduli of the rubbers were determined from the respective stress strain curves. Since, the modulus is found to vary with the strain level, the compression modulus was obtained only for the low strain range ( $0 \sim 0.25$ ), for which the stress-strain relations were found linear. The measured relations in the above strain range were thus well approximated by the corresponding best-fit straight lines, the slopes of which ultimately give the required moduli. The compression modulus of tire and natural rubbers so obtained in our present study was 7.10 MPa and 5.23 MPa, respectively. Note that the value of the modulus of tire rubber, used in the analysis of Huh and Kwak (1990), was 5.49 MPa, which is quite close to that obtained for our natural rubber. Therefore, the measured material properties of tire and natural rubber have been used in the following analysis of tire-tread contact problem.

## 5 Results and Discussions

### 5.1 General

In this section, the solutions of the tire-tread stress problem are presented for two limiting cases of the contact condition - one assumes free lateral slippage and the other conforms to the no-slip condition of the surface in contact with the road. In the case of free-slippage condition, the solution of the problem is obtained without considering the influence of any friction on the tread surface in contact. That is, the tread contact surface will be allowed to deform freely both in normal and lateral directions, without experiencing any frictional resistance from the road surface. The geometry and loading used for the solution of the tire-tread stress problem is illustrated in Fig. 2. The relevant boundary conditions of the frictionless contact problem, which have been satisfied by different segments of the tread section, are listed in Table 1(a). Table 1(b) illustrates the scheme for managing the boundary conditions at the corner points of the tread section, which are, in general, the points of singularity. On the other hand, the no-slip condition of the contact boundary is referred to the case where the available frictional resistance from the road surface is assumed to be sufficiently high, so that the lateral displacement of the boundary, caused by the application of the uniform normal compression from the road surface is restrained. For the solution of the present no-slip contact problem, the management of the boundary conditions for different segments of the tread boundary as well as for the associated corner points is illustrated in Tables 2(a) and 2(b), respectively.

Table 1(a): Specification of the boundary conditions for the tire-tread contact problem considering free-slippage of the contact boundary

Boundary segment*	Given boundary conditions	Tagging of boundary conditions	
		Mesh point on the physical boundary	Mesh point on the imaginary boundary
AB	$[u_n, \sigma_t]$	$\sigma_t$	$u_n$
BC	$[\sigma_n, \sigma_t]$	$\sigma_t$	$\sigma_n$
CD	$[\sigma_n, \sigma_t]$	$\sigma_n$	$\sigma_t$
DE	$[u_n, \sigma_t]$	$u_n$	$\sigma_t$
EF	$[u_n, u_t]$	$u_t$	$u_n$
FG	$[u_n, \sigma_t]$	$u_n$	$\sigma_t$
GH	$[\sigma_n, \sigma_t]$	$\sigma_n$	$\sigma_t$
AH	$[\sigma_n, \sigma_t]$	$\sigma_t$	$\sigma_n$

\* Refer to Fig. 2

Table 1(b): Boundary condition modeling for the corner points of the tread section, corresponding to Table 1(a)

Corner point *	Given boundary conditions	Used conditions	Tagging of boundary conditions	
			Mesh point on the physical boundary	Mesh points on the imaginary boundary
A	$[(u_n, \sigma_t), (\sigma_n, \sigma_t)]$	$[\sigma_t, u_n, \sigma_t]$	$\sigma_t$	$[u_n, \sigma_t]$
B	$[(u_n, \sigma_t), (\sigma_n, \sigma_t)]$	$[\sigma_t, u_n, \sigma_t]$	$\sigma_t$	$[u_n, \sigma_t]$
D	$[(u_n, \sigma_t), (\sigma_n, \sigma_t)]$	$[u_n, \sigma_t, \sigma_n]$	$u_n$	$[\sigma_t, \sigma_n]$
G	$[(u_n, \sigma_t), (\sigma_n, \sigma_t)]$	$[u_n, \sigma_t, \sigma_n]$	$u_n$	$[\sigma_t, \sigma_n]$
E	$[(u_n, u_t), (u_n, \sigma_t)]$	$[u_t, u_n, \sigma_t]$	$u_t$	$[u_n, \sigma_t]$
F	$[(u_n, u_t), (u_n, \sigma_t)]$	$[u_t, u_n, \sigma_t]$	$u_t$	$[u_n, \sigma_t]$
C	$[(\sigma_n, \sigma_t), (\sigma_n, \sigma_t)]$	$\sigma_n$	$\sigma_n$	–
H	$[(\sigma_n, \sigma_t), (\sigma_n, \sigma_t)]$	$\sigma_n$	$\sigma_n$	–

\* Refer to Fig. 2

Table 2(a): Specification of the boundary conditions for the tire-tread stress problem conforming to the no-slip condition of the contact boundary

Boundary segment *	Given boundary conditions	Tagging of boundary conditions	
		Mesh point on the physical boundary	Mesh point on the imaginary boundary
AB	$[u_n, u_t]$	$u_t$	$u_n$
BC	$[\sigma_n, \sigma_t]$	$\sigma_n$	$\sigma_t$
CD	$[\sigma_n, \sigma_t]$	$\sigma_n$	$\sigma_t$
DE	$[u_n, \sigma_t]$	$u_n$	$\sigma_t$
EF	$[u_n, u_t]$	$u_t$	$u_n$
FG	$[u_n, \sigma_t]$	$u_n$	$\sigma_t$
GH	$[\sigma_n, \sigma_t]$	$\sigma_n$	$\sigma_t$
AH	$[\sigma_n, \sigma_t]$	$\sigma_n$	$\sigma_t$

\* Refer to Fig. 2

Instead of using the uniformly distributed pressure from the road surface, the contact boundary is subjected to the equivalent uniform normal displacement, which ensured better accuracy and stability of the finite-difference solution. The uniform normal displacement considered in the present analysis corresponds to the internal inflation pressure of the tire, for example, 100 psi (690 kPa). The condition of the contact boundary experiencing frictionless slippage is modeled here by assigning a uniform value to the normal displacement and zero value to the tangential stress component for all the nodal points on the boundary (see Table 1). And, the contact boundary conforming to the no-slip condition is modeled by assigning a uniform

Table 2(b): Boundary condition modeling for the corner points of the tread section, corresponding to Table 2(a) (Case-A)

Corner point *	Given boundary conditions	Used conditions	Tagging of boundary conditions	
			Mesh point on the physical boundary	Mesh points on the imaginary boundary
A	$[(u_n, u_t), (\sigma_n, \sigma_t)]$	$[u_n, u_t, \sigma_n]$	$u_t$	$[u_n, \sigma_n]$
B	$[(u_n, u_t), (\sigma_n, \sigma_t)]$	$[u_n, u_t, \sigma_n]$	$u_t$	$[u_n, \sigma_n]$
D	$[(u_n, \sigma_t), (\sigma_n, \sigma_t)]$	$[u_n, \sigma_t, \sigma_n]$	$u_n$	$[\sigma_n, \sigma_t]$
G	$[(u_n, \sigma_t), (\sigma_n, \sigma_t)]$	$[u_n, \sigma_t, \sigma_n]$	$u_n$	$[\sigma_n, \sigma_t]$
E	$[(u_n, u_t), (u_n, \sigma_t)]$	$[u_t, u_n, \sigma_t]$	$u_t$	$[u_n, \sigma_t]$
F	$[(u_n, u_t), (u_n, \sigma_t)]$	$[u_t, u_n, \sigma_t]$	$u_t$	$[u_n, \sigma_t]$
C	$[(\sigma_n, \sigma_t), (\sigma_n, \sigma_t)]$	$\sigma_n$	$\sigma_n$	–
H	$[(\sigma_n, \sigma_t), (\sigma_n, \sigma_t)]$	$\sigma_n$	$\sigma_n$	–

\* Refer to Fig. 2

value to the normal component and zero value to the tangential component of displacement (see Table 2). In all cases, displacements are normalized with respect to the contact length ( $a$ ) and stresses are normalized with respect to the contact pressure ( $P$ ) applied to the contact boundary from the road surface (see Fig. 2).

## 5.2 Deformed Shape

The deformed shape of a tread section ( $a/b = 1.5$ ) obtained for the frictionless slip-page of the contact boundary is shown in Fig. 4(a) along with the original tread section which is subjected to a contact pressure of 690 kPa. As appears from the figure, the solution conforms to almost all the physical requirements of the model. The overall accuracy of the solution is also verified to be better than that obtained with the applied normal stress on the contact boundary. It has also been verified that the same normal compressive stress is reproduced along the contact boundary when the problem is solved in terms of its equivalent uniform normal displacement. Figure 4(b) shows the original and deformed shapes of the tire-tread section conforming to the no-slip condition of the contact boundary, under the same contact pressure of 690 kPa. The tread section is found to be inflated under the action of the uniform displacement, leaving the contact boundary free from lateral displacement, which is in good agreement with the physical characteristic of the model. The lateral displacement component takes its maximum value around the mid-depth position of the skid surfaces, AE and BD. The solutions are obtained for the treads of natural rubber and actual tire rubber, and the corresponding deformed shapes are included in the same Figs. of 4(a) and (b). The solutions show that the deformed state of the tire tread section differs significantly from that of the natural rubber,

which signifies the importance of the appropriate material properties for predicting the state of deformation in the tread section.

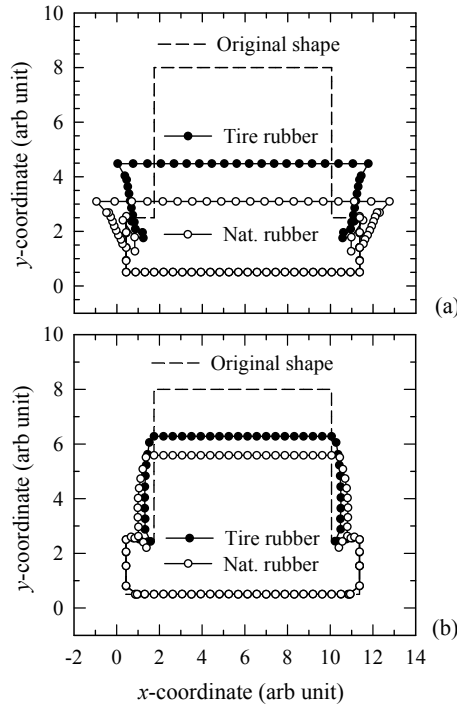


Figure 4: Deformed shapes of the tire tread section ( $a/b = 1.5$ ) under (a) free-slippage and (b) no-slip conditions of the contact boundary (displacements are magnified)

When the contact surface of the tread section is subjected to uniform pressure from the road surface, symmetric lateral displacement around the mid-point of the contact boundary is happened together with the normal displacement. This lateral displacement eventually causes the lateral slippage of the surface in contact with the road. In absence of friction between the tread surface and the road, the lateral slipping gets its maximum value. However, when the frictional resistance is present, the frictional force tends to oppose the lateral displacement of the contact boundary, and eventually it will prevent the displacement completely when the resistance is sufficiently high. Figure 5 shows the distribution of lateral displacement along the contact surface of the tread section ( $a/b = 1.5$ ) for the above two limiting cases of tire and natural rubbers; all other cases related to practical slippage will be in between the two limiting cases.

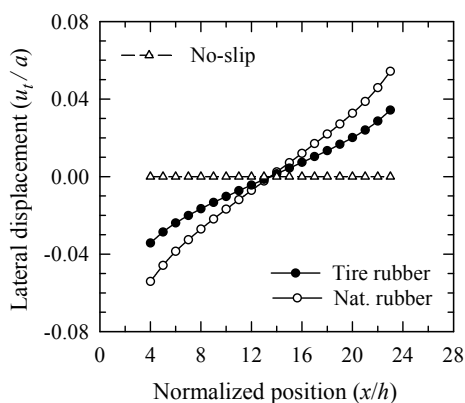


Figure 5: Lateral displacement along the contact boundary of the tire tread sections ( $a/b = 1.5$ ) under no-slip and free-slippage conditions

### 5.3 Solution of Stresses

#### Stresses at the contact boundary

Figure 6 presents the solutions of different components of stress along the contact boundary of the tread section ( $a/b = 1.5$ ) subjected to a contact pressure of 690 kPa. As mentioned in Table 2(b), the available conditions for the two corner nodal points of the no-slip contact boundary, AB are  $u_n$ ,  $u_t$ ,  $\sigma_n$ , and  $\sigma_t$ . First, out of these four boundary conditions, three conditions, namely,  $u_n$ ,  $u_t = 0$ , and  $\sigma_n = 0$  (referred to here as ‘Case–A’), are satisfied at both the corner points of the contact boundary. As is seen from the distribution of the resulting shearing stress in Fig. 6(a), the magnitude of the stress at the two corner points of the boundary show extremely higher value compared to those of the remaining section. In an attempt to predict a more refined value of the corner shearing stress, the same problem is solved by satisfying another possible set of conditions ( $u_n$ ,  $u_t = 0$ , and  $\sigma_t = 0$ ; referred to as ‘Case–B’) at the two corner points of the boundary. In this case, however, exactly zero shearing stresses are found to occur at the corner points, leaving the remaining section almost identical with that of Case–A. Although the prediction of this zero shearing stress at the corners is accurate from the view point of numerical solution, it is realized to be inconsistent with the solution of Fig. 5, as, at the extreme two points of the contact boundary, the lateral displacement was found to take its maximum value in absence of the shearing stresses. The two solutions, Case–A & Case–B, as obtained for the tire tread section,  $a/b = 1.5$ , are illustrated on the same graph of Fig. 6(a). It is clear from the figure that the solutions differ only at the corner points, and thus the effect of singularity on the

solution is highly localized. In order to obtain a more justified value of the shear stress at the corner points of the contact boundary, the corner stresses are predicted by extrapolating the distribution keeping the slope of the curve near the corners the same. The extrapolated curves of shearing stress for the no-slip contact boundaries of tire and natural rubber treads are also shown in Fig. 6(a); the stress level for the case of natural rubber is found to be higher than that in the actual tire-tread.

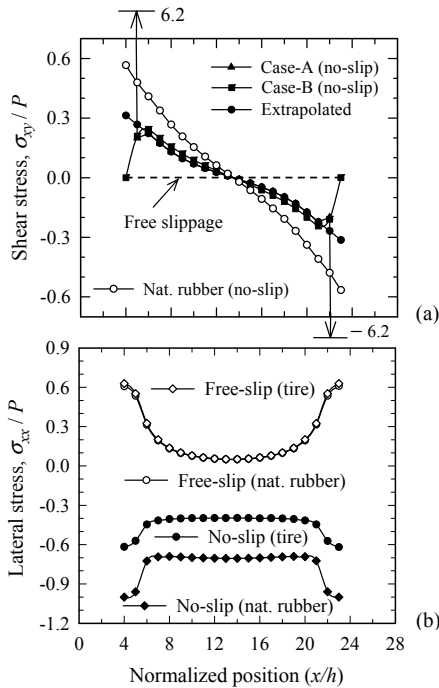


Figure 6: Stresses along the contact boundary of the tire tread section ( $a/b = 1.5$ ): (a) shear stress under no-slip condition, (b) normal stress under no-slip and free-slip conditions

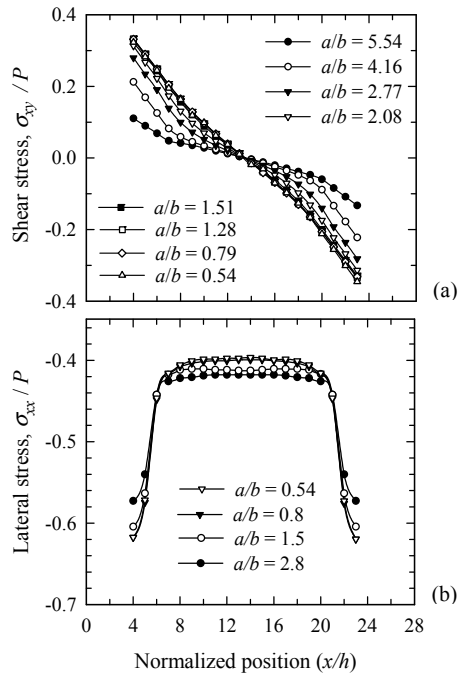


Figure 7: Influence of aspect ratio (skid depth,  $b$ ) on the stresses along the contact boundary of tire tread, under no-slip condition: (a) shear stress, (b) lateral stress

The distributions of lateral stress component,  $\sigma_{xx}$  along the contact boundary of the tread section are shown in Fig. 6(b). The solutions for the free-slippage (no friction) and no-slip conditions of the contact boundary are obtained for both the materials of tire and natural rubbers, which are shown in the same graph. As far as the present stress component is concerned, the entire contact boundary is under compression for the case of no-slip condition, however, the same is found under tension when the free-slippage condition of the boundary is adopted in the solution.

For the case of free slippage condition, the mid-region of the contact boundary is almost free from stresses and the associated magnitude of the stress increases gradually as we move towards the corner regions of the boundary. Moreover, the effect of material properties is found to be insignificant for the free-slippage lateral stress along the contact boundary, as the two distributions are found identical in terms of both shape and magnitude (see Fig. 6(b)); however, on the other hand, a different phenomenon is observed for the case of no-slip condition. When the lateral displacement along the boundary is restricted (no-slip condition), the lateral stress developed at the contact boundary is found to differ significantly from that of the free-slippage condition. It is noted here that the lateral stress induced due to the application of no-slip condition on the contact boundary is found to be higher for the case of natural rubber. This may be attributed to the phenomenon that the free-slippage lateral displacement along the contact boundary was much higher for the tread of natural rubber compared to that of tire rubber (see Fig. 5), even though both of them were subjected to identical contact pressure from the road surface.

The effect of tread aspect ratio on the distribution of stresses along the contact boundary, conforming to the no-slip condition, is illustrated in Fig. 7. Figure 7(a) illustrates the distribution of shear stress along the contact boundary of tread sections having different aspect ratios, where the skid depth is varied keeping the contact length the same. At the middle portion of the contact boundary, shear stress is found to be zero for all the tread sections. Away from the middle portion, magnitude of shear stress increases up to its maximum value towards the corner points of the boundary; shearing stresses at the two corners are almost equal in magnitude but opposite in sense. In general, the shearing stress increases with the decrease of aspect ratio, *i.e.*, with the increase of skid depth, and becomes almost saturated for lower values of aspect ratio. Moreover, the nonlinearity of the distribution along the contact boundary is found to decrease with the increase of skid depth. From Fig. 7(b), it is observed that the magnitude of lateral stress,  $\sigma_{xx}$  increases with the increase of skid depth of the tire tread up to a certain limit. Over the ranges  $4 \leq x/h \leq 7$  and  $19 \leq x/h \leq 23$ , the lateral stress,  $\sigma_{xx}$  varies significantly and, as a result, the highest lateral stress is developed at the corner points of the contact boundary.

Fig. 8 describes the relationship between the maximum coefficient of friction and aspect ratio of tire-tread sections for both the materials of tire and natural rubbers. This relationship, in turn, provides important information regarding the amount of friction required from the road surface to keep the tread section free from lateral slippage. It is noted here that, this lateral slippage of the contact boundary plays one of the major roles in shortening the life of tires as far as the abrasion loss is concerned (Ahmed *et al.*, 2005b). Here, according to the Coulomb's law of fric-

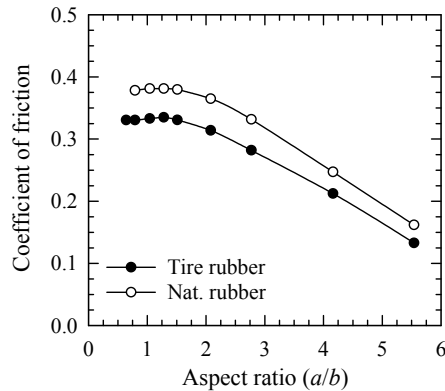


Figure 8: Maximum coefficient of friction as a function of tire tread aspect ratio, under no-slip condition of the contact boundary

tion, the coefficient of friction is obtained by dividing the no-slip shearing stress developed on the contact surface by the associated contact pressure. The general trend of the relation of Fig. 8 reveals that the maximum coefficient of friction increases with the increase of skid depth and it becomes nearly saturated for higher values of the depth for both the materials of tires and natural rubber. From the figure it is also observed that tire tread of natural rubber shows higher coefficient of friction compared to the tread of tire material, which is because the lateral slippage of the contact boundary of the tread of natural rubber under no frictional resistance is found to be higher than that of tire rubber (see Fig. 5). In other words, the tread sections of natural rubber would require higher frictional resistance from the road surface to keep them free from lateral slippage. The results of the present analysis thus reveal that both the geometrical parameters and material properties of tire treads play major roles in determining their performance against abrasion due to lateral slippage on the road surface.

#### Stresses at the tread shoulder

Fig. 9 presents the variation of different stress components along the shoulder region of the tire-tread section ( $a/b = 1.5$ ) subjected to a contact pressure of 690 kPa. Solutions for the case of no-slip condition of the contact boundary of treads of natural rubber and actual tire material are presented in a comparative fashion in the same graph. It has been verified in our present study that no significant change in the solution of stresses at the shoulder section is encountered when the contact boundary assumes the condition of free lateral slippage without any frictional resistances. Figure 9(a) illustrates the distribution of shearing stress component at

the shoulder section of the tire treads. For both the natural rubber and tire material, the shear stress distribution is anti-symmetric and the associated highest stresses are developed at the two re-entrant corners of the shoulder section, H and C (see Fig. 2). Except for the two corner points, shear stress varies almost linearly over the shoulder section, where the solutions for the two materials are found to be very close to each other. Figure 9(b) presents the distribution of lateral stress,  $\sigma_{xx}$  at the shoulder section of the treads. The two re-entrant corners are found here to be almost free from lateral stress; however, the maximum lateral stress at the shoulder section is found to occur at the immediate neighbor to the corner points. Although the entire shoulder section is under compression for both the tread materials, the magnitude of lateral stress developed for the case of natural rubber is higher than that in tire rubber. Figure 9(c) illustrates the distribution of the normal stress,  $\sigma_{yy}$  at the shoulder section for two types of tire materials. At the shoulder section, both the normal and lateral stresses are compressive in nature. Except for the two corner regions, the normal stress is found to distribute almost uniformly over the section, where the stress level for the case of natural rubber is higher than that in the tire rubber. Among the three stress components, this normal stress component is identified to be highly sensitive to the singularity associated with two re-entrant corner points, as the stresses at the corner points are found to assume much higher values (more than 5 to 6 times) than the pressure acting on the contact boundary. From the results of the present analysis, the corner regions of the shoulder section are identified to be the most critical sections in terms of stresses within the entire tread section; otherwise, the overall stress level at the contact boundary is found higher than that at the shoulder section.

## 6 Finite Element Solution and Comparison

Finite-element solution of the present tire-tread contact problem has been obtained for the two limiting conditions of the contact boundary. The solutions are obtained using the standard facilities of the commercial FEM software ANSYS. The four-noded rectangular plane elements are used to model the tire-tread sections. Likewise the case of our FDM solution, the element density is kept uniform all over the domain, where all the elements are of same size. The total number of finite elements used to construct the corresponding FEM mesh-network for the tread section ( $a/b = 1.5$ ) was 450 ( $25 \times 18$ ), which is somewhat similar to that used in the FDM discretization. The convergence as well as the accuracy of the solution has also been verified by varying the element density.

Figures 10-12 show the comparison of solutions of different stress components at different regions of the tire-tread section under no-slip as well as free-slippage conditions, obtained by the two methods, namely FDM and FEM. Figures 10(a) and

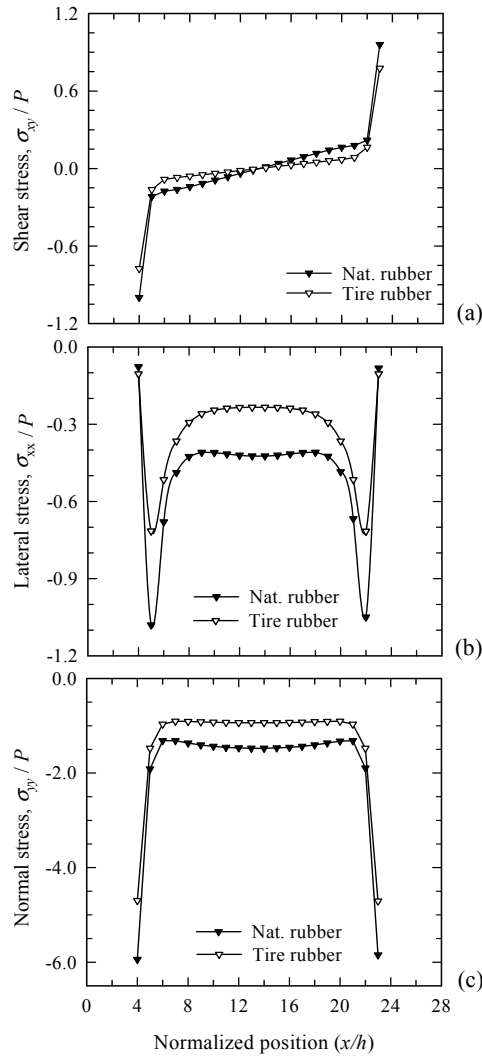


Figure 9: Distribution of stress components at the shoulder section of the tire tread ( $a/b = 1.5$ ) under no-slip condition: (a) shear stress, (b) lateral stress, (c) normal stress

(b) show the comparison of the two solutions for the lateral and shear stresses at the shoulder section of the no-slip tire-tread. For most of the points of the section, the two solutions for the stresses obtained by the completely two different approaches are found to be in excellent agreement with each other in terms of both

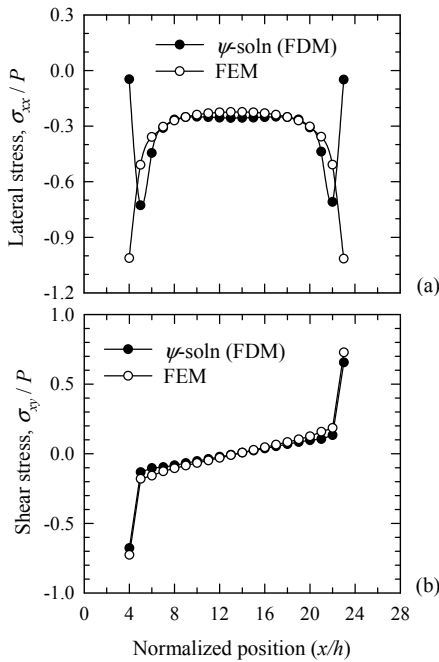


Figure 10: Comparison of stresses along the shoulder section of the tire tread section ( $a/b = 1.5$ ) under no-slip condition: (a) lateral stress, (b) shear stress

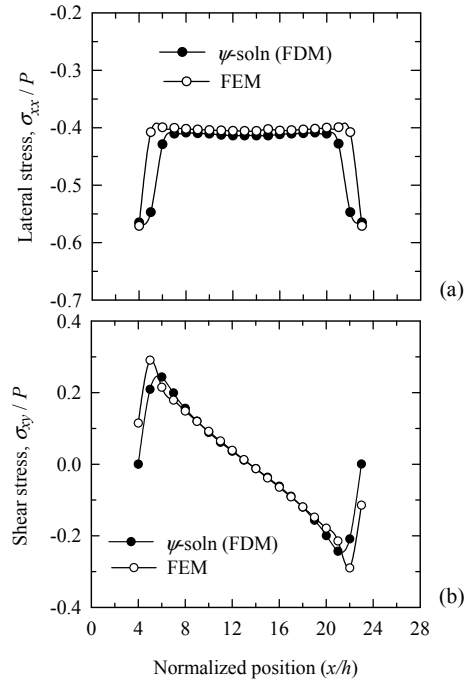


Figure 11: Comparison of stresses along the contact boundary of the tire tread section ( $a/b = 1.5$ ) under no-slip condition: (a) lateral stress, (b) shear stress

magnitude and nature of variation; slight discrepancies are appeared mainly at the corner points, which are basically because of the different ways of handling the associated corner singularities. Further, from the results of Figs. 11 (a) and (b), the two solutions for both the lateral and shear stress at the no-slip contact boundary, respectively, are also found, in general, to be in good conformity with each other. Here, the original solutions of shear stress distribution, which are free from the application of extrapolation scheme to the corner regions, are presented in Fig. 11(b). Likewise the case of shoulder section, the discrepancies between the two solutions are also observed mainly around the corner regions of the contact boundary, however, they are found to be more pronounced than those at the shoulder section. As appears from Fig. 11(b), the present FDM solution reproduces the zero shearing stress at the corners exactly, which, in turn, reflects the capability of the present computational method in reproducing the conditions at the boundary (Case-

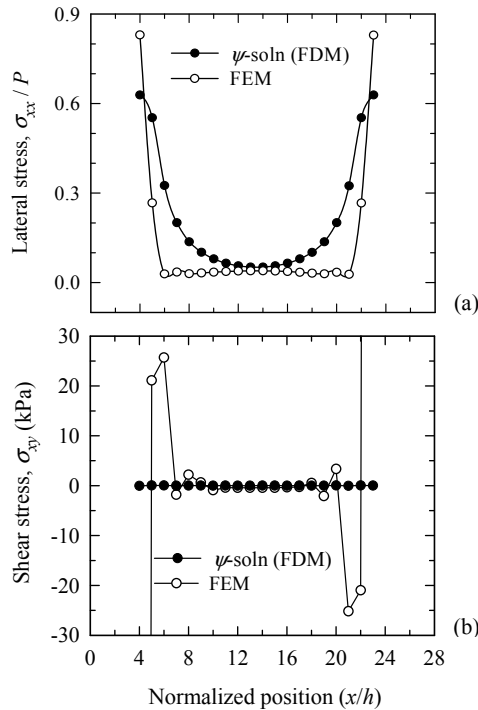


Figure 12: Comparison of stresses along the contact boundary of the tire-tread section ( $a/b = 1.5$ ) under free-slippage condition: (a) lateral stress, (b) shear stress

B). The FEM solution has however yielded a nonzero shearing stress at the corners, which assumes a value around  $\pm 70$  kPa. Further, a comparison of the solutions for stresses at the contact boundary, when it is free to deform in both normal and lateral directions under contact pressure without any frictional resistances, shows that the distributions obtained by the two methods differ quite significantly (see Fig. 12). Instead of assuming a smooth distribution of the lateral stress component, the FE solution shows the section concerned is almost free from lateral stress except for the two extreme regions (see Fig. 12(a)). This FE prediction of the lateral stress may be doubtful as it does not conform to the associated deformation characteristics; from both the deform shape (Fig. 4(a)) and the distribution of lateral displacement (Fig. 5) it is realized that the boundary deforms laterally from its center point to two opposite directions in a gradual manner, and the deformation gets its highest value at the extreme corners. This deformation phenomenon has however been reflected appropriately by the corresponding lateral stress distribution obtained by the present FD solution. The superiority of the present FDM in reproducing the stresses along

the bounding surfaces is also illustrated in Fig. 12(b); the figure shows the state of shear stress along the contact boundary of the tread. The boundary is basically free from any shearing stress and the corresponding state of stress is reproduced exactly by the present method. However, the FEM solution is found to assume a peculiar anti-symmetric distribution of the shear stress at the contact boundary, which is highly unlikely; solutions for a total of five to six nodes from both the corner points are suffering from severe inaccuracy. Since the modeling of the boundary conditions for the corner points in usual FE simulation does not take into account the effect of singularity, the predictions near the corner regions may be unreliable. On the other hand, the transition of boundary conditions in our FD modeling is handled in a more justified way, in which, for each of the external corner points of the tread section, a total of three conditions out of the available four are satisfied appropriately (see Table 1(b)). As a result, the present solutions are claimed to be closer to the actual state of stresses and thus highly reliable.

## 7 Conclusions

A simplified analysis of the tire-tread contact problem has been carried out in an attempt to predict deformation as well as stresses at different critical sections of tire-tread section using the displacement potential based finite-difference technique. The solution of the problem is obtained here for two limiting cases of the contact boundary, from which other intermediate cases of interest can readily be interpolated. Both the qualitative and quantitative results as well as the comparison with the usual computational method firmly establish the reliability as well as superiority of the present results, which are thus expected to be of great help for accurate and economic design of tires. In the present analysis, the two re-entrant corners of the tread shoulder section are identified to be the most critical regions in terms of stresses; otherwise, the overall stress level at the contact boundary is higher than that of any other sections in the tread. Further, it has been realized that both material properties and geometrical parameters of the tread section would have significant influence on the service life of treads, as the frictional resistance required from the road surface to keep the contact boundary free from lateral slippage is found to depend on them substantially.

## References

- Ahmed, S. R.; Hossain, M. Z.; Uddin, M. W.** (2005a): A general mathematical formulation for finite-difference solution of mixed-boundary-value problems of anisotropic materials. *Computers & Structures*, vol. 83, pp. 35–51.
- Ahmed, S. R.; Idris, A. B. M.; Uddin, M.W.** (1996): Numerical solution of both

ends fixed deep beams. *Computers & Structures*, vol. 61(1), pp. 21–29.

**Ahmed, S. R.; Khan, M. R.; Islam, K. M. S.; Uddin, M. W.** (1998): Investigation of stresses at the fixed end of deep cantilever beams. *Computers & Structures*, vol. 69, pp. 329–338.

**Ahmed, S. R.; Nath, S. K. D.; Uddin, M. W.** (2005b): Optimum shapes of tire-treads for avoiding lateral slippage between tires and roads. *International Journal for Numerical Methods in Engineering*, vol. 64, pp. 729–750.

**Akanda, M. A. S.; Ahmed, S. R.; Uddin, M. W.** (2002): Stress analysis of gear teeth using displacement potential function and finite differences. *International Journal for Numerical Methods in Engineering*, vol. 53, pp. 1629–1640.

**Aliabadi, M. H.** (2002): *The Boundary Element Method: Volume 2 Applications in Solids and Structures*. John Wiley & Sons, Chichester, England.

**ASTM Standard D4014–89**: Standard Specification for Plain and Steel-Laminated Elastomeric Bearings of Bridges, ANNEX A1. Determination of Shear Modulus, 1–6.

**Atluri, S. N.; Shen, S. P.** (2002): *The meshless local Petrov-Galerkin (MLPG) method*. Tech. Science Press.

**Bathe, K. J.; Chaudhary, A.** (1984): On finite element analysis of large deformation frictional contact problem. Unification of Finite Element Methods (Edited by H. Kardestuncer), North-Holland, Amsterdam, pp. 123–135.

**Benito, J. J.; Ureña, F.; Gavete, L.; Alonso, B.** (2008): Application of the generalized finite difference method to improve the approximated solution of pdes. *CMES: Computer Modelling in Engineering & Sciences.*, vol. 38, pp. 39–58.

**Campos, L. T.; Oden, J. T.; Kikuchi, N.** (1982): A numerical analysis of a class of contact problems with friction in elastostatics, *CMES: Computer Methods in Applied Mechanics & Engineering*, vol. 34, pp. 821–845.

**Criado, R.; Ortiz, J. E.; Mantić, V.; Gray, L. J.; Paris, F.** (2007): Boundary element analysis of three-dimensional exponentially graded isotropic elastic solids. *CMES: Computer Modelling in Engineering & Sciences.*, vol. 22, pp. 151–164.

**Dow, J.; Jones, M. S.; Harwood, S. A.** (1990): A new approach to boundary modeling for finite difference applications in solid mechanics. *International Journal for Numerical Methods in Engineering*, vol. 30, pp. 99–113.

**Huh, H.; Kwak, Y. K.** (1990): Finite element stress analysis of the reinforced tire contact problem. *Computers & Structures*, vol. 36 (5), pp. 871–881.

**Libre, N. A.; Emdadi, A.; Edward, J. K.; Rahimian, M.; Shekarchi, M.** (2008): A stabilized RBF collocation scheme for Neumann type boundary value problems. *CMES: Computer Modelling in Engineering & Sciences.*, vol. 24, pp. 61–80.

**Mohenimanesh, A.; Ward, S. M.; Gilchrist, M. D.** (2009): Stress analysis of a multi-laminated tractor tyre using non-linear 3D finite element analysis. *Materials and Design*, vol. 30 (4), pp. 1124–1132.

**Nath, S. K. D.; Ahmed, S. R.** (2009): Displacement Potential Solution of Stiffened Composite Struts Subjected to Eccentric Loading. *Journal of Applied Mathematical Modeling*, vol. 33 (3), pp. 1761–1775.

**Noor, K.; Tanner, J. A.** (1985): Advances and trends in the development of computational models for tires. *Computers & Structures*, vol. 20, pp. 517–533.

**Oden, J. T.; Becker, E. B.; Lin, T. L.; Demkowicz, L.** (1984): Formulation and finite element analysis of a general class of rolling contact problems with finite elastic deformation. *Mathematics of Finite Elements with Applications*, vol. V, (Edited by J. R. Whiteman), Academic, London.

**Oden, J. T.; Pires, E. B.** (1983): Numerical analysis of certain contact problems in elasticity with non-classical friction laws. *Computers & Structures*, vol. 16, pp. 481–485.

**Pahr, D. H.; Böhm, H. J.** (2008): Assessment of mixed uniform boundary conditions for predicting the mechanical behavior of elastic and inelastic discontinuously reinforced composites. *CMES: Computer Modelling in Engineering & Sciences.*, vol. 34, pp. 117–136.

**Pahr, D. H.; Zysset, P. K.** (2008): Influence of boundary conditions on computed apparent elastic properties of cancellous bone. *Biomechanics and Modeling in Mechanobiology*, vol. 7 (6), pp. 463–476.

**Rothert, H.; Gall, R.** (1986): On the three-dimensional computation of steel-belted tires. *Tire Science and Technology*, vol. 14, pp. 116–124.

**Tabaddor, F.; Stafford, J. R.** (1985): Some aspects of rubber composite finite element analysis. *Computers & Structures*, vol. 21 (1/2), pp. 327–339.

**Tan, C. I.; Shiah, Y. C.; Lin, C. W.** (2009): Stress analysis of 3D generally anisotropic elastic solids using the boundary element method. *CMES: Computer Modelling in Engineering & Sciences.*, vol. 41, pp. 195–214.

**Timoshenko, S.; Goodier, J. N.** (1979): *Theory of Elasticity*, 3rd Ed., McGraw-Hill Book Company, New York.

**Tonti, E.; Zarantonello, F.** (2009): Algebraic formulation of elastostatics: the Cell method. *CMES: Computer Modelling in Engineering & Sciences.*, vol. 39, pp. 201–236.

**Vignjevic, R.; Vuyst, T. D.; Campbell, J. C.** (2006): A frictionless contact algorithm for meshless methods. *CMES: Computer Modelling in Engineering & Sciences.*, vol. 13, pp. 35–48.

**Wang, T. M.; Daniel, I. M.; Huangn, K.** (1996): Stress analysis of tire sections. *Tire Science and Technology*, vol. 24 (4), pp. 349–366.

**Zhang, X.; Rakheja, S.; Ganesan, R.** (2002): Stress analysis of the multi-layered system of a truck-tire. *Tire Science and Technology*, vol. 30 (4), pp. 240–264.

### List of Symbols

$\psi(x, y)$	Displacement potential function
$E$	Modulus of Elasticity
$\mu$	Poisson's ratio
$u_x, u_y$	Displacement components in $x$ and $y$ directions
$\sigma_{xx}$	Lateral stress in $x$ direction
$\sigma_{yy}$	Normal stress in $y$ direction
$\sigma_{xy}$	Shear stress
$u_n, u_t$	Normal and tangential components of displacement
$\sigma_n, \sigma_t$	Normal and tangential components of stress
$a$	Tread contact length
$b$	Skid depth
$h, k$	Mesh lengths in $x$ and $y$ directions
$P$	Contact pressure

